Foundations for Gravitational Potential Energy Evaluation

Nicolas Poupart

Independent Researcher

E-mail: nicolas.poupart@yahoo.fr

Abstract. We investigate the evaluation of effective gravitational binding energy in heterogeneous stellar systems and compare a permutation-invariant exact estimator with heuristic sequential formulations. The exact estimator provides a physically consistent reference based on additive contributions and volume-conserving mergers, whereas the heuristic formulation introduces a path dependence that can strongly modify the reconstructed dark-to-baryonic mass ratios.

A systematic exploration of stellar-population permutations quantifies this sensitivity and shows that optimized orderings can substantially reduce the bias of the heuristic approximation. Using SPARC-based reconstructions together with GALEX and SDSS photometric tests, we show that the apparent numerical advantage of the heuristic method is partly artificial when it is evaluated against the exact energy. A simplified reconstruction program nevertheless demonstrates that similarly high dynamical success rates can be recovered when the exact estimator is used directly during optimization.

These results establish the exact estimator as the physical baseline for effective gravitational binding energy, while showing that the success of the reconstruction is driven primarily by the underlying physical constraint rather than by algorithmic sophistication.

Keywords: galaxies: kinematics and dynamics, galaxies: structure, dark matter, gravitation, methods: numerical, methods: statistical, rotation curves

Contents

1 Introduction

This article extends the previous study *"Dark Mass is Potential Energy"* [1], in which the idea of Léon Brillouin [2, 3] was developed, according to which relativistic dynamics should be renormalized by potential energy. This hypothesis, formulated prior to the observational establishment of flat galactic rotation curves [4, 5], proposed an elegant interpretation of the phenomenon. However, Brillouin did not succeed in establishing a rigorous method for renormalizing potential energy, and this natural explanation fell into oblivion because general relativity does not possess a covariant expression for gravitational energy [6] and therefore complicates the formulation of a global conservation law for gravitational energy.

The renormalization of the field $\Phi(M)$ produced by the potential energy of a set of masses M can be simply interpreted as $\Phi(\gamma M)$, in other words as if the mass M were multiplied by

a renormalization factor γ. For an observer, this renormalization could be perceived as the effect of an additional baryonic mass:

$$\gamma' \ \Phi(M) = \Phi(\gamma M) = \Phi(M) + \Phi(DM)$$

where DM would then be interpreted as invisible dark matter. This hypothesis corresponds to the current standard cosmological model [7].

In general relativity, the gravitational field is identified with the curvature of spacetime; therefore, renormalization must be understood as an increase in this curvature. Nevertheless, there exists a terminological ambiguity between "mass", "matter", and "spacetime curvature". We often say that mass gravitates and curves spacetime, although more precisely it is energy, in all its forms, that acts as the source of curvature [8]. This curvature manifests itself as an effect commonly designated by the term "mass". Thus, if effective gravitational binding energy curves spacetime and generates an effective mass, this contribution does not necessarily act as an additional source term within the renormalized description, thereby preventing an iterative growth of the field. The extent to which gravitational binding energy may contribute to the effective mass of galaxies, however, has not yet been quantitatively established.

That this renormalization exists seems to have been numerically demonstrated by A. Deur [9–12], who argues (numerically) that the self-interaction of the gravitational field by its own energy density can produce a curvature of spacetime capable of explaining dark mass. However, these works do not make it possible to describe cosmological phenomena analytically in a simple manner. They nevertheless illustrate how gravitational binding energy generates an additional curvature that can be interpreted as an additional "mass" or as an effective renormalization of mass.

Our work uses Newtonian gravitation (NG) to calculate this field renormalization and obtain simple analytical expressions. Purists will object that this is not general relativity (GR), since we employ neither tensor mathematics nor Einstein's equations. However, it is mathematically indisputable that NG derives from GR in the weak-field approximation [6], and thus results derived in NG are consistent with GR in the weak-field regime. The essential advantage of this approach is that, within the Newtonian framework, effective gravitational binding energy is well defined–which makes it possible, thanks to our previous work, to deduce a correct analytical expression for the real total potential energy of a system.

However, the behavior of the evaluation of the correct energy differs from that of the heuristic we have used. We will analyze the different algorithmic alternatives for evaluating effective gravitational binding energy and their implications.

The objective of this article is therefore to clarify the role of algorithmic choices in the evaluation of effective gravitational binding energy and in the reconstruction of stellar populations from galactic rotation data. In particular, this work makes three contributions.

First, we introduce a permutation-invariant formulation that provides an exact macroscopic estimator of gravitational binding energy for heterogeneous stellar systems. This estimator establishes a physically consistent reference independent of the ordering of stellar populations. Second, we analyze the heuristic sequential formulation used in our previous work and quantify its sensitivity to the ordering of stellar components through systematic permutation studies. Third, we investigate the role of the optimization algorithm itself, showing that the high reconstruction performance observed in practice is primarily driven by the underlying physical constraint rather than by the heuristic approximation. Together, these results clarify the respective roles of physics and algorithmic structure in the reconstruction of galactic stellar populations from dynamical data.

2 Exact Evaluation of the Effective Gravitational Binding Energy

We now introduce a computation scheme for effective gravitational binding energy that is both structurally linear and invariant under permutation of the constituent mass intervals. The objective is not to revisit the full theoretical construction developed previously [1], but rather to formalize a calculation procedure that preserves the physical additivity of energy while remaining independent of the ordering of stellar populations.

2.1 Linear construction of the binding energy

Consider a system decomposed into n mass intervals characterized by densities ρ_i and total masses M_i. Each interval is constructed from individual self-gravitating stars sharing the same density and is then treated as an equivalent compact sphere whose radius follows directly from mass conservation:

$$R_i = \left(\frac{3M_i}{4\pi\rho_i}\right)^{1/3} \tag{2.1}$$

The gravitational binding energy associated with this compact configuration defines a natural macroscopic energy scale:

$$\Delta E_i = \frac{3G}{5}\frac{M_i^2}{R_i} \tag{2.2}$$

Crucially, this contribution depends only on intrinsic properties of the interval and therefore enters the total energy as a strictly additive term. The system is then updated by merging this compact sphere with the previously accumulated configuration (M_c, R_c) according to volume conservation:

$$M_c \leftarrow M_c + M_i, \qquad R_c \leftarrow \left(R_c^3 + R_i^3\right)^{1/3} \tag{2.3}$$

The process is repeated sequentially for all intervals, yielding a linear accumulation of energy contributions:

$$\Delta E_{\text{tot}} = \sum_{i=1}^{n} \Delta E_i + \frac{3G}{5}\frac{M_n^2}{R_n} \tag{2.4}$$

The final term represents the binding energy of the global compact configuration obtained after all mergers. In practice, it remains of the same order of magnitude as the individual interval contributions but never dominates the total energy, typically accounting for only a few percent (typically 1%-5%).

2.2 Physical and mathematical consistency of the energy estimate

The proposed evaluation of the effective gravitational binding energy is supported by three complementary arguments.

First, it follows directly from a physically grounded construction applied consistently across scales. The macroscopic energy scale GM^2/R is obtained by starting from individual stars, each treated as a self-gravitating sphere, and by aggregating them into compact configurations through volume-conserving mergers. Stellar populations are therefore not introduced as abstract blocks but emerge from the same physical logic that governs the elementary constituents. The conservative nature of the gravitational field ensures that the resulting binding energy depends only on the final configuration and not on the assembly path, while volume conservation prevents the introduction of artificial forces or unphysical density variations. The calculation thus remains firmly anchored in standard gravitational physics.

Second, the method possesses a consistent mathematical structure. The total energy is obtained through strictly additive contributions, while the final result is invariant under permutation of the mass intervals. This dual property guarantees that the estimate is independent of any arbitrary ordering of stellar populations and therefore reflects an intrinsic property of the mass distribution rather than an artifact of the algorithm.

Third, the approach demonstrates strong empirical adequacy. When applied to observed stellar populations, the resulting energy scale is empirically supported by comparisons with SPARC-based reconstructions and GALEX/SDSS photometric validations. This convergence between theoretical construction and observational constraints provides an additional indication that the estimator captures the dominant gravitational physics at galactic scales.

2.3 Algorithmic structure

Because each interval contributes through an intrinsic energy scale before being merged, the total energy depends only on the collection $\{(M_i, \rho_i)\}$ and not on the order in which the intervals are processed.

Formally, let σ be any permutation of $\{1, \ldots, n\}$. The cumulative radius after all mergers satisfies:

$$R_c^3 = \sum_{i=1}^{n} R_{\sigma(i)}^3 = \sum_{i=1}^{n} R_i^3 \tag{2.5}$$

which immediately implies that the final compact state (M_n, R_n) is unique. Since the additive contributions ΔE_i are themselves independent of ordering, the total energy remains unchanged under permutation.

This property reflects the conservative nature of the gravitational field: the binding energy is determined solely by the final mass distribution and not by the path taken to assemble it.

The resulting procedure is characterized by two essential features: (i) linearity, whereby each density class contributes an autonomous energy term, preserving the transparency of the mass–energy budget; and (ii) permutation invariance, ensuring that the final result is independent of the sequencing of stellar populations and therefore physically consistent.

Together, these properties define an exact macroscopic estimator of effective gravitational binding energy suitable for heterogeneous stellar systems.

3 Heuristic Evaluation of Effective Gravitational Binding Energy

Having established the permutation-invariant estimator, we now introduce the heuristic algorithm employed in our previous work. This procedure was preferred because it produced better empirical agreement with observations (SPARC [13]).

3.1 Algorithmic construction

Consider a stellar population described by a density ρ and total mass M, merged with an existing compact configuration (M_i, R_i). The algorithm updates the global configuration according to:

$$f(\rho, M, M_i, R_i) \to \left\{ \begin{array}{ll} M_t & = M + M_i \\ R & = \left(\dfrac{3M}{4\pi\rho}\right)^{1/3} \\ R_t & = \left(R^3 + R_i^3\right)^{1/3} \\ \Delta E_{\rm pi} & = \dfrac{3GM_t^2}{5R_t} \end{array} \right\} \to (\Delta E_{\rm pi}, M_t, R_t) \tag{3.1}$$

At each step, the incoming stellar population is first represented as an equivalent compact sphere obtained through volume conservation. The merged radius R_t then defines the characteristic gravitational scale of the updated system, from which the energy contribution is evaluated using the macroscopic form GM^2/R.

3.2 Closed-form expression as a sum

Let the n intervals be characterized by $(\rho_i, M_i)_{1\le i\le n}$, and let $(M_0, R_0) = (0, 0)$. Define the equivalent compact radius of each interval by:

$$R_i \;=\; \left(\frac{3M_i}{4\pi\rho_i}\right)^{1/3} \tag{3.2}$$

For a chosen ordering σ of $\{1, \ldots, n\}$, define the cumulative mass–radius sequence by:

$$M_j \;=\; M_{j-1} + M_{\sigma(j)}, \qquad R_j^3 \;=\; R_{j-1}^3 + R_{\sigma(j)}^3, \qquad j = 1, \ldots, n \tag{3.3}$$

so that $R_j = \left(\sum_{\ell=1}^{j} R_{\sigma(\ell)}^3\right)^{1/3}$ and $M_j = \sum_{\ell=1}^{j} M_{\sigma(\ell)}$. The heuristic algorithm assigns at step j the energy:

$$\Delta E_j^{(\sigma)} \;=\; \frac{3G}{5}\,\frac{M_j^2}{R_j} \tag{3.4}$$

The heuristic total is therefore the path-dependent sum:

$$\Delta E_{\rm heur}^{(\sigma)} \;=\; \sum_{j=1}^{n} \Delta E_j^{(\sigma)} \;=\; \frac{3G}{5} \sum_{j=1}^{n} \frac{\left(\sum_{\ell=1}^{j} M_{\sigma(\ell)}\right)^2}{\left(\sum_{\ell=1}^{j} R_{\sigma(\ell)}^3\right)^{1/3}} \tag{3.5}$$

This expression makes explicit that the heuristic estimate depends on the permutation σ through the partial sums in both mass and volume.

3.3 Interpretation

Unlike the exact linear construction introduced previously, this heuristic method evaluates the binding energy of the updated global configuration at every merger step. The procedure therefore attributes to each interval an energy that already incorporates its coupling with the previously accumulated mass.

This choice has two important consequences. First, the algorithm naturally captures the dominant gravitational scale of the system without requiring the explicit computation of intercoupling terms. Second, it introduces a path dependence: since the energy is evaluated on partially assembled configurations, the final result can vary with the ordering of the stellar populations.

This path dependence is in fact a defining strength of the heuristic estimator. The interdependence introduced at each merger step increases the sensitivity of the energy to the assembly sequence, thereby strongly constraining the space of admissible trajectories when constructing stellar populations. As a consequence, greedy optimization procedures tend to converge naturally toward a restricted set of stable solutions, whereas a fully additive formulation permits a much larger family of equivalent configurations. This controlled reduction of degeneracy makes the heuristic scheme particularly effective for recovering physically plausible stellar distributions from observational constraints.

4 Comparison of the Exact and Heuristic Estimators

We compare the permutation-invariant estimator (hereafter the *exact* method) with the heuristic algorithm within the same optimization framework applied to the SPARC dataset. For each galaxy, the algorithm searches for stellar mass distributions capable of reproducing the inferred dark mass by matching the predicted effective gravitational binding energy to the observational constraints, while enforcing the bounds $P \pm k\sigma$ on the stellar fractions. The tolerance parameter k therefore controls the accessible region of parameter space and directly impacts the solvability of the rotation-curve data.

In this work, a kinematic point is considered solved when the reconstructed dark mass falls within the observational uncertainty interval associated with the corresponding rotation-curve measurement. The optimization procedure itself minimizes the relative error between the predicted gravitational binding energy and the inferred dark mass, but the success criterion reported in the tables is based on the absolute observational error bars. A galaxy is considered solved when all of its kinematic points satisfy this condition.

Table 1 summarizes the fraction of resolved kinematic points and fully solved galaxies obtained with each estimator as a function of k, allowing a direct assessment of how the structural differences between the two energy formulations affect the convergence of the greedy search and the recovery of observationally consistent stellar populations.

Two distinct initial stellar populations are considered in this comparison. The first corresponds to the reference stellar distribution described above. The second introduces an additional gas-clumping component and is invoked only when the first population fails to produce a satisfactory solution. This extended model is primarily intended to resolve intermediate spiral galaxies with extended disks and low gas content.

4.1 Resolution performance

Across all tolerance levels, the heuristic estimator systematically resolves a larger fraction of both individual points and galaxies. The difference is modest at 1σ, where both methods operate under strong constraints, but becomes pronounced as the admissible parameter space expands.

At 2σ, the contrast is already significant: the heuristic method nearly doubles the number of solved galaxies when the second distribution is included. The effect becomes decisive at 3σ, where the heuristic algorithm approaches full resolution of the dataset, exceeding 99% of solved points and more than 93% of galaxies, while the exact estimator remains close to the 50% level.

4.2 Origin of the performance gap

This discrepancy follows directly from the structural differences between the two estimators. The exact formulation is strictly additive and permutation-invariant, which implies that many stellar configurations produce comparable energy levels. While mathematically consistent, this enlarged degeneracy weakens the sensitivity of the optimization process and makes convergence toward observationally compatible populations more difficult.

By contrast, the heuristic estimator introduces controlled path dependence. Because each merger step modifies the global gravitational scale, the admissible trajectories through parameter space become strongly constrained. This increased sensitivity acts as an implicit regularization mechanism for greedy optimization procedures, guiding them toward a restricted subset of stable solutions.

Table 1. Comparison of resolution as a function of the k-factor and method used

	First Distribution		**With Second Distribution**	
k **method**	**Points Solved**	**Galaxies Solved**	**Points Solved**	**Galaxies Solved**
1σ Exact	746 (24.5%)	18 (10.3%)	809 (26.5%)	25 (14.4%)
1σ Heuristic	790 (25.9%)	22 (12.6%)	1082 (35.5%)	29 (16.7%)
2σ Exact	1207 (39.6%)	59 (33.9%)	1309 (43.0%)	67 (38.5%)
2σ Heuristic	1372 (45.0%)	82 (47.1%)	3010 (98.8%)	158 (90.8%)
3σ Exact	1560 (51.2%)	93 (53.4%)	1514 (49.7%)	93 (53.4%)
3σ Heuristic	1930 (63.3%)	107 (61.5%)	3022 (99.1%)	162 (93.1%)

4.3 Photometric validation: GALEX and SDSS correlations

Beyond the purely dynamical resolution rates reported in Table 1, the two estimators can be compared through an independent photometric validation. For each reconstructed stellar population, we compute synthetic ultraviolet and optical colors and test their correspondence with GALEX and SDSS observations [14–18] using Pearson and Spearman correlation analyses.

Table 2 summarizes the predicted–observed correlations obtained with the exact and heuristic estimators for four color indices. The comparison is performed in identical conditions (same galaxy sets and same statistical procedures), so that differences can be attributed to the structure of the energy estimator and its impact on the recovered stellar populations.

Overall, both methods produce statistically significant ordering relations across multiple bands, confirming that dynamical constraints alone can generate structured stellar population mixtures. However, the relative performance depends on the wavelength range and on whether linear or rank-based correlations are considered.

For the optical $g-r$ color, the heuristic estimator yields the strongest monotonic ordering, with a Spearman coefficient $\rho_S = 0.611$ (8.66σ), compared to $\rho_S = 0.490$ (6.30σ) for the exact method. A similar improvement is observed for the mixed UV–optical color NUV–r, where the heuristic approach increases both Pearson and Spearman correlations. These two indices are the most sensitive to the global population balance between low-mass main-sequence stars and denser components, and the heuristic path dependence appears to provide the additional selectivity required for robust cross-galaxy ordering.

Table 2. Correlation analysis between predicted and observed galaxy colors. Pearson r and Spearman ρ coefficients are reported together with their Gaussian-equivalent significances. Linear fits are reported in rank–rank space.

Color	N	r_{P}	σ_{P}	ρ_{S}	σ_{S}	$b_{\mathrm{rank}} \pm 1\sigma$
$g-r$ Exact	128	0.430	5.34	0.490	6.30	0.490 ± 0.078
$g-r$ Heuristic	128	0.483	6.19	0.611	8.66	0.611 ± 0.071
NUV–r Exact	119	0.461	5.62	0.546	7.04	0.546 ± 0.077
NUV–r Heuristic	119	0.522	6.63	0.586	7.83	0.586 ± 0.075
$r-z$ Exact	129	0.212	2.45	0.430	5.36	0.430 ± 0.080
$r-z$ Heuristic	129	0.325	3.88	0.393	4.81	0.393 ± 0.082
FUV–NUV Exact	136	-0.152	1.78	-0.263	3.16	-0.263 ± 0.083
FUV–NUV Heuristic	136	-0.049	0.57	-0.313	3.82	-0.313 ± 0.082

For the $r-z$ optical color, the situation is inverted: the exact estimator provides a slightly stronger rank correlation $\rho_{\mathrm{S}} = 0.430$ (5.36σ) than the heuristic method $\rho_{\mathrm{S}} = 0.393$ (4.81σ), corresponding to a significance ratio of ~ 1.1 (Gaussian-equivalent), while the heuristic improves the Pearson coefficient. This indicates that both reconstructions encode a meaningful optical ordering, but with different trade-offs between monotonic ranking and linear coherence in raw color space.

Finally, the purely ultraviolet color FUV–NUV remains the least monotonic indicator for both methods. Both estimators produce only moderate anticorrelations, with the heuristic method exhibiting a weaker Pearson coefficient but a stronger Spearman coefficient. This behavior is consistent with the known multi-regime structure of ultraviolet colors, where distinct star-formation histories can overlap in integrated UV indices and naturally weaken global monotonic trends.

Taken together, these results show that the heuristic estimator tends to enhance the recoverability of population ordering from dynamics, particularly in $g-r$ and NUV–r, while the exact estimator can remain competitive in specific optical bands. This reinforces the interpretation advanced above: the permutation-invariant estimator provides a structurally rigorous energy scale, whereas the heuristic estimator introduces a controlled dependence that acts as an effective constraint on the reconstruction and can improve convergence toward observationally consistent stellar population orderings.

4.4 Interpretation

The comparison highlights a fundamental trade-off between mathematical invariance and algorithmic efficiency. The exact estimator provides a structurally rigorous definition of the gravitational binding energy, whereas the heuristic method behaves as a powerful inference operator capable of rapidly identifying stellar populations consistent with observational constraints.

In practice, the strong empirical performance of the heuristic approach suggests that the induced trajectory constraint captures relevant physical structure within the stellar distribution. Rather than being a drawback, the path dependence appears to supply the level of selectivity required for large-scale galactic reconstruction.

5 Analysis of the Sensitivity of the Heuristic

The reconstruction begins from a reference stellar population spanning a wide range of intrinsic densities, from diffuse main-sequence stars to ultra-compact remnants. The components include black holes (BH), neutron stars (NS), white dwarfs (WD), red giants (RG), and the standard spectral classes from O to M. This basis is not intended to reproduce a detailed stellar census; rather, it provides a physically motivated density spectrum capable of generating the gravitational energy required by the dynamical constraints. Since the energy response is strongly non-linear with respect to density, different permutations of the same components can lead to distinct reconstruction trajectories, making the ordering itself an object of study rather than an imposed assumption.

For nearby galaxies ($z \approx 0$), consistent with the populations represented in SPARC, we adopt average mass fractions normalized to unity:

$$\begin{array}{lll} \mathrm{BH} = 1.0\% \pm 0.5\% & \mathrm{NS} = 0.3\% \pm 0.1\% & \mathrm{WD} = 2.2\% \pm 0.7\% \\ \mathrm{RG} = 0.2\% \pm 0.1\% & \mathrm{M} = 55\% \pm 10\% & \mathrm{K} = 16\% \pm 6\% \\ \mathrm{G} = 10.5\% \pm 5\% & \mathrm{F} = 5.5\% \pm 3\% & \mathrm{A} = 5\% \pm 2\% \\ \mathrm{B} = 3\% \pm 1\% & \mathrm{O} = 1.3\% \pm 0.5\% & \end{array}$$

These fractions reflect the well-established dominance of low-mass stars in the stellar mass budget, while compact remnants provide a small but dynamically significant contribution. The ordered list [BH, NS, WD, RG, M, K, G, F, A, B, O] will hereafter be referred to as the original (or initial) ordering, as it corresponds to the sequence adopted in our previous work.

5.1 Permutation analysis

Figure 1 displays the ratio DM/M_{bar} produced by 1×10^5 different permutations of the stellar population ordering. A broad fluctuation band is observed, spanning from a minimum ratio of 0.8 to a maximum of 128, illustrating the strong dependence of the heuristic estimator on the chosen population sequence.

The permutation corresponding to strictly increasing density yields an exceptionally large ratio of 120.5, whereas the strictly decreasing density ordering produces a much lower value of 1.9. The original ordering adopted in our previous work yields 50.2, whereas the exact value is 55.6 for all permutations, corresponding to an error of approximately 10%.

Across all permutations, the median ratio is 12, while the mean reaches 21.4, revealing a strongly skewed distribution with a long high-ratio tail that significantly shifts the mean. Overall, this figure highlights the pronounced sensitivity of the heuristic estimator to the ordering of stellar populations.

5.2 Proportion analysis

Figure 2 shows the relative error in the dark-to-baryonic mass ratio obtained with the heuristic estimator compared to the exact method for the original permutation. The histogram is generated from 1×10^5 distinct stellar fractions satisfying the 1σ constraint.

The error spans approximately from -20% to -5%, revealing a systematic bias in the heuristic prediction. Applying a rescaling factor of 1.1 to the dark mass computed with the heuristic estimator reduces this offset and shifts the error interval to roughly -10% to 5%. After this adjustment, the distribution becomes nearly centered, with a mean relative error of -1.2% and a median of -0.6%.

Figure 1. Distribution of the predicted dark-to-baryonic mass ratio across 1×10^5 stellar population permutations. Each bin groups the permutations yielding ratios within the corresponding range, highlighting the strong sensitivity of the heuristic estimator to population ordering.

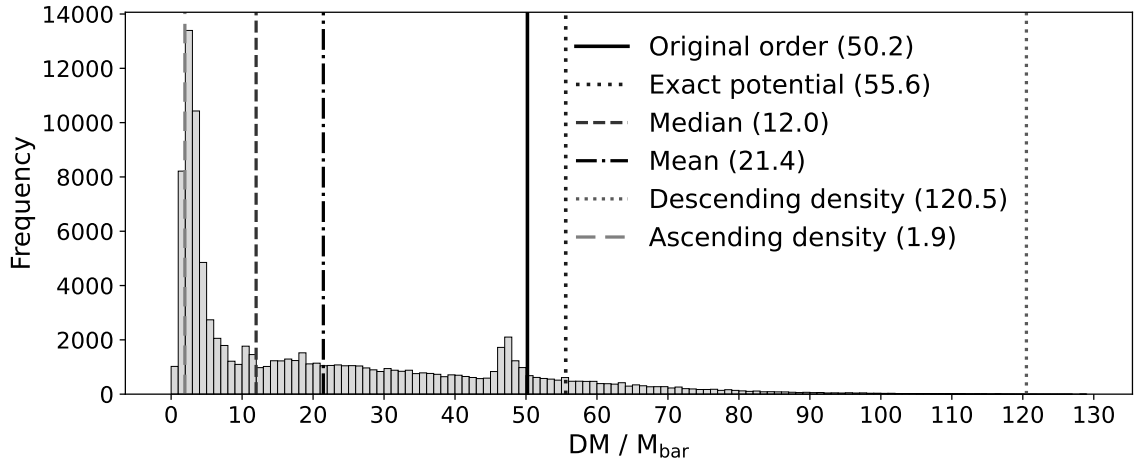

Figure 3 shows the error histogram obtained for the permutation [NS, A, WD, B, K, BH, M, RG, G, F, O], identified through a greedy search starting from the original ordering. The improvement is immediately visible: a simple scaling by 1.01 is sufficient to center the distribution on zero.

The resulting error closely follows a Gaussian profile, spanning approximately from -5% to 5%, which indicates that the systematic bias observed for the original permutation has effectively disappeared.

Figure 2. Distribution of the relative error in the dark-to-baryonic mass ratio between the heuristic and exact estimators for the original permutation under the 1σ constraint, computed from 1×10^5 stellar fraction realizations. The thick black line indicates the median of the distribution, while the dashed lines mark the $\pm 1\sigma$, $\pm 2\sigma$, and $\pm 3\sigma$ intervals.

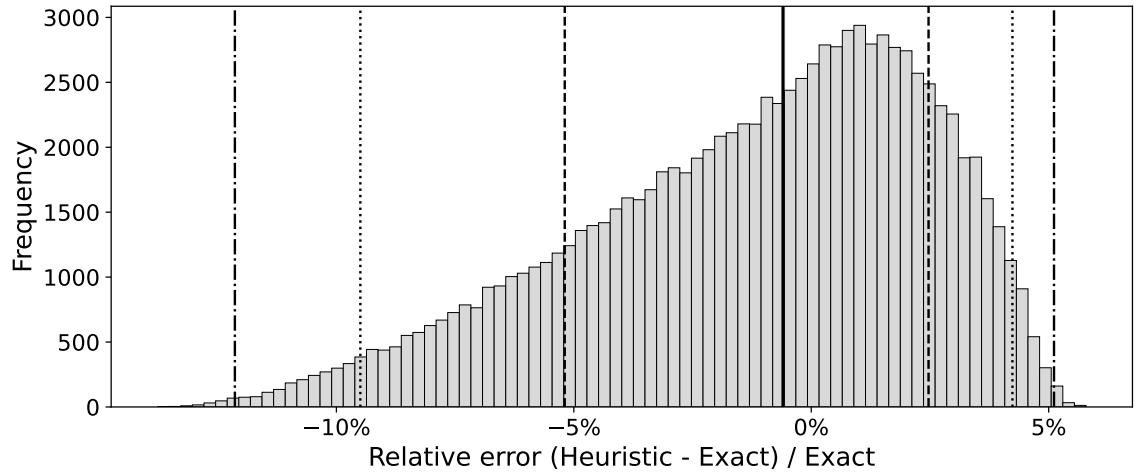

Figure 3. Distribution of the relative error in the dark-to-baryonic mass ratio between the heuristic and exact estimators for the permutation [NS, A, WD, B, K, BH, M, RG, G, F, O] under the 1σ constraint, computed from 1×10^5 stellar fraction realizations. The thick black line indicates the median of the distribution, while the dashed lines mark the $\pm 1\sigma$, $\pm 2\sigma$, and $\pm 3\sigma$ intervals.

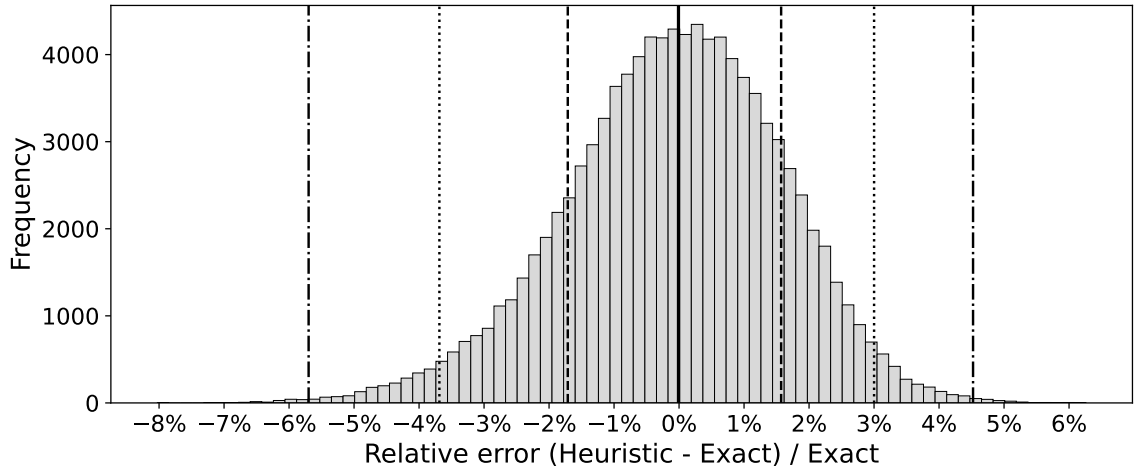

5.3 Comparison of the old and new heuristic estimators

Tables 3 and 4 compare the performance of the exact estimator with two heuristic implementations that differ solely by the ordering of the stellar populations. The underlying algorithm, physical assumptions, and parameter space are strictly identical; only the permutation is modified.

Table 3 shows that both heuristic variants significantly outperform the exact estimator in terms of resolved kinematic points and solved galaxies. The old heuristic achieves the highest resolution rates, particularly when the second distribution is included, solving nearly all data points at 2σ. The new heuristic remains very close to this performance, with only a modest reduction in convergence efficiency.

Because the algorithm itself is unchanged, these differences directly quantify the impact of population ordering on the heuristic reconstruction. The results therefore provide empirical evidence of the strong path dependence introduced by the sequential structure of the estimator.

Table 4 further evaluates the statistical consistency of the reconstructed populations through correlations between predicted and observed galaxy colors. For the optical $g - r$ and mixed NUV–r indices, both permutations produce statistically significant monotonic relations that remain broadly comparable to those obtained with the exact estimator. The new permutation yields slightly lower Pearson and Spearman coefficients than the old ordering, yet the correlations remain robust, indicating that the global ordering of galaxies is largely preserved.

For the $r - z$ color, the exact estimator retains the strongest rank correlation, whereas both heuristic permutations exhibit weaker but still significant trends. By contrast, the FUV–NUV index shows the strongest correlation for the new permutation, exceeding both the old ordering and the exact estimator in Spearman significance. Since the underlying algorithm is otherwise identical, this result indicates that ultraviolet ordering is particularly sensitive to the sequence in which stellar components are aggregated.

Taken together, these results show that permutation alone can measurably affect both convergence efficiency and photometric ordering without altering the overall statistical coherence of the reconstruction. The heuristic estimator is therefore not defined solely by its mathematical form, but also by the trajectory it follows through population space, suggesting that the reconstruction path itself constitutes an intrinsic component of sequential gravitational energy models.

Table 3. Comparison of resolution as a function of the k-factor and method used

	First Distribution		**With Second Distribution**	
k **method**	**Points Solved**	**Galaxies Solved**	**Points Solved**	**Galaxies Solved**
1σ Exact	746 (24.5%)	18 (10.3%)	809 (26.5%)	25 (14.4%)
1σ Old	790 (25.9%)	22 (12.6%)	1082 (35.5%)	29 (16.7%)
1σ New	750 (24.6%)	18 (10.3%)	965 (31.7%)	27 (15.5%)
2σ Exact	1207 (39.6%)	59 (33.9%)	1309 (43.0%)	67 (38.5%)
2σ Old	1372 (45.0%)	82 (47.1%)	3010 (98.8%)	158 (90.8%)
2σ New	1240 (40.7%)	67 (38.5%)	2980 (97.8%)	148 (85.1%)
3σ Exact	1560 (51.2%)	93 (53.4%)	1514 (49.7%)	93 (53.4%)
3σ Old	1930 (63.3%)	107 (61.5%)	3022 (99.1%)	162 (93.1%)
3σ New	1614 (53.0%)	102 (58.6%)	3014 (98.9%)	163 (93.7%)

5.4 Search-space analysis

Our hypothesis that non-linear heuristics reduce the effective search space can be tested by explicitly counting the number of branching possibilities encountered by the algorithm.

Table 4. Correlation analysis between predicted and observed galaxy colors. Pearson r and Spearman ρ coefficients are reported together with their Gaussian-equivalent significances. Linear fits are reported in rank–rank space.

Color	N	r_{P}	σ_{P}	ρ_{S}	σ_{S}	$b_{\mathrm{rank}} \pm 1\sigma$
$g-r$ Exact	128	0.430	5.34	0.490	6.30	0.490 ± 0.078
$g-r$ Old	128	0.483	6.19	0.611	8.66	0.611 ± 0.071
$g-r$ New	128	0.446	5.59	0.523	6.89	0.523 ± 0.076
NUV–r Exact	119	0.461	5.62	0.546	7.04	0.546 ± 0.077
NUV–r Old	119	0.522	6.63	0.586	7.83	0.586 ± 0.075
NUV–r New	119	0.440	5.30	0.476	5.86	0.476 ± 0.081
$r-z$ Exact	129	0.212	2.45	0.430	5.36	0.430 ± 0.080
$r-z$ Old	129	0.325	3.88	0.393	4.81	0.393 ± 0.082
$r-z$ New	129	0.194	2.23	0.378	4.60	0.378 ± 0.082
FUV–NUV Exact	136	-0.152	1.78	-0.263	3.16	-0.263 ± 0.083
FUV–NUV Old	136	-0.049	0.57	-0.313	3.82	-0.313 ± 0.082
FUV–NUV New	136	-0.216	2.56	-0.338	4.15	-0.338 ± 0.081

The first stage of the greedy procedure consists of a linear exploration in which stellar fractions are adjusted individually. Only modifications that decrease the reconstruction error are retained, each representing a potential branching point in the search trajectory. Among these admissible branches, the algorithm systematically selects the one producing the largest improvement. The number of such branching possibilities was therefore recorded for each configuration.

When no further improvement can be achieved through single-parameter adjustments, the algorithm transitions to a quadratic exploration phase, where pairs of stellar fractions are modified simultaneously. As in the linear stage, only error-reducing combinations are preserved, each defining a new branching possibility, and the algorithm again selects the most favorable candidate. The number of admissible quadratic branches was likewise measured.

The results reported in Table 5 reveal a clear structural effect of the heuristic constraints on the effective search region explored by the greedy algorithm.

For the linear exploration phase, both heuristic formulations substantially reduce the number of admissible branching possibilities compared to the exact estimator. The reduction is already visible when a single initial population is used, but becomes markedly stronger when two populations are introduced. This behavior indicates that the path dependence induced by the heuristic rapidly restricts the set of viable trajectories through parameter space, thereby guiding the optimization toward a narrower subset of solutions.

The situation differs for the quadratic phase. While the exact estimator continues to explore a relatively large number of two-parameter combinations, the original heuristic (old) is in several cases surpassed by the exact method. This suggests that the constraint imposed by the original ordering may become excessively restrictive once the algorithm reaches higher-order adjustments, potentially limiting its ability to escape local minima.

By contrast, the new permutation maintains a reduced search region while avoiding the strongest over-constraining effects observed in the old configuration. This balance indicates that population ordering does not merely influence convergence speed, but directly shapes the topology of the accessible parameter space.

Taken together, these results support the interpretation that non-linear heuristic structure acts as an implicit regularization mechanism: it suppresses large portions of the search space during early exploration while preserving enough flexibility to allow higher-order corrections when necessary.

This behavior further suggests that the reconstruction trajectory is not merely an algorithmic artifact, but a structurally important component of gravitational binding energy reconstruction.

6 Importance of the Algorithm

To better understand the role played by the different algorithmic variants, we developed a new reconstruction program in which all factors can be explicitly controlled. The implementation was deliberately simplified so that every step of the procedure remains fully transparent and easily interpretable. In this framework, the variation of stellar populations is strictly bounded and no stellar fraction can ever exceed the limits $P \pm k\sigma$ during the optimization process. The minimized quantity is the relative error between the reconstructed gravitational binding energy and the inferred dark mass. This quantity is used only to guide the optimization procedure, whereas the final success criterion for a kinematic point is determined by the observational error bars of the rotation-curve data.

Table 5. Comparison of the fraction of parameter space explored by the greedy algorithm under linear (X) and quadratic (X^2) exploration.

	With One Distribution		**With Two Distributions**	
k **method**	X	X^2	X	X^2
1σ Exact	61.5%	13.4%	85.3%	11.0%
1σ Old	31.0%	60.3%	6.2%	100.0%
1σ New	44.0%	11.6%	15.9%	32.9%
2σ Exact	100.0%	33.7%	100.0%	50.6%
2σ Old	47.4%	100.0%	4.9%	30.6%
2σ New	76.4%	24.8%	6.4%	20.4%
3σ Exact	87.2%	29.0%	85.6%	68.2%
3σ Old	39.9%	68.7%	4.5%	24.1%
3σ New	74.1%	10.8%	5.1%	20.2%

6.1 Consequence on the usefulness of the heuristic

The apparent superiority of the heuristic estimator observed in the previous sections must be interpreted with caution. The heuristic formulation does not compute the exact gravitational binding energy but rather a path-dependent approximation used internally by the optimization procedure. As a consequence, the high success rate obtained when the heuristic value is used as the convergence criterion partly reflects the fact that the algorithm is evaluated using the same approximate quantity that it attempts to reproduce.

When the heuristic estimator is used, the new program simultaneously computes two quantities: the heuristic value used by the algorithm to reach convergence and the corresponding exact energy obtained from the permutation-invariant formulation. This makes it possible to measure directly the discrepancy between the two estimators for each reconstructed configuration.

Table 6 summarizes the reconstruction statistics obtained when the algorithm converges using the heuristic value. Although the heuristic evaluation suggests an extremely high success rate, the comparison with the exact estimator reveals that a large fraction of these apparently successful reconstructions do not reproduce the true binding energy precisely. This comparison shows that the apparent performance of the heuristic estimator is partly artificial: it reflects the internal consistency of the approximation rather than the physical correctness of the reconstructed energy.

Table 6. Comparison between heuristic and exact evaluations for identical reconstructed configurations.

Method	**Points Without Error**	**Galaxies Without Error**
Heuristic Evaluation	2982 (97.83%)	149 (85.63%)
Exact Evaluation	974 (31.96%)	41 (23.56%)
Exact Optimization	2983 (97.87%)	149 (85.63%)

The same algorithm was then executed while using the exact gravitational binding energy directly during the optimization process. Remarkably, the reconstruction performance remains essentially identical to the heuristic-based convergence. This result demonstrates

Table 7. Correlation analysis between predicted and observed galaxy colors obtained with the simplified reconstruction program. Pearson r and Spearman ρ coefficients are reported together with their Gaussian-equivalent significances.

Color	N	r_{P}	σ_{P}	ρ_{S}	σ_{S}
FUV–NUV Exact	136	-0.340	4.19	-0.390	4.90
FUV–NUV Heuristic	136	-0.260	3.12	-0.310	3.78
$r-z$ Exact	171	0.111	1.45	0.433	6.24
$r-z$ Heuristic	171	0.052	0.68	0.323	4.44
$g-r$ Exact	170	0.218	2.90	0.360	5.00
$g-r$ Heuristic	170	0.244	3.25	0.340	4.69
NUV–r Exact	138	0.234	2.81	0.531	7.31
NUV–r Heuristic	138	0.319	3.93	0.647	9.91

that the high resolution rates observed previously are not intrinsically tied to the heuristic approximation itself. When the exact energy is used as the optimization target, the greedy procedure remains capable of converging toward solutions of comparable quality.

To verify that the reconstructed stellar populations remain astrophysically realistic, we performed the same photometric validation used throughout this work by comparing predicted galaxy colors with GALEX and SDSS observations using Pearson and Spearman correlation analyses. Table 7 summarizes the correlations obtained for both the exact and heuristic reconstructions.

These correlations confirm that the stellar populations reconstructed with the exact estimator remain statistically consistent with observed galaxy colors. While the heuristic reconstruction sometimes produces slightly stronger correlations in specific bands, the exact formulation performs comparably across most color indices and even improves the ultraviolet correlations.

Taken together, these results show that the success of the reconstruction procedure does not fundamentally depend on the heuristic approximation itself. The heuristic estimator mainly acts as a computational shortcut that accelerates convergence, while the exact estimator retains the physically rigorous definition of the gravitational binding energy. The efficiency of the reconstruction therefore appears to arise primarily from the structure of the greedy search and from the physical constraints imposed on the stellar populations.

6.2 Gas Clumping Treatment

A major improvement of the new algorithm lies in the treatment of gas clumping, which is now both simpler, more transparent, and more efficient. In the previous implementation, gas clumping was handled implicitly through the use of two distinct stellar populations, one of which introduced clumping in an essentially ad hoc manner. In the present formulation, the clumping factor is introduced explicitly through a continuous parameter:

$$M_{\mathrm{bar}} = M_{\mathrm{stars}} + M_{\mathrm{gas}}$$

$$DM = \mathrm{ComputeExactPotentialEnergy}\big(M_{\mathrm{bar}}(1 - \mathrm{GasClumping})\big)$$

The parameter GasClumping $\in [0, 1]$ therefore directly controls the effective contribution of the gas component to the gravitational binding energy.

A value of 0 corresponds to a configuration in which the gas follows the same spatial distribution as the stellar component. When the clumping factor remains smaller than the gas mass fraction, the gas is effectively more concentrated than the stars and produces its own gravitational binding energy that is lower than that associated with the stellar profile. Conversely, when the clumping factor exceeds the gas fraction, the spatial distribution of the gas dominates the effective gravitational profile.

Table 8 summarizes the statistical properties of the reconstructed galaxies depending on whether gas clumping is required by the optimization procedure.

Table 8. Statistical properties of galaxies reconstructed with and without gas clumping.

Quantity	**Minimum**	**Maximum**	**Mean $\pm\sigma$**	**Median**
Galaxies With Gas Clumping (62)				
Clumping Factor (%)	2.3	93.5	59.8 ± 24.2	64.8
Gas Fraction (%)	2.3	77.2	22.4 ± 16.5	17.8
Relative Error (no clumping)	-2.1×10^{-6}	14.5	3.066 ± 3.780	1.638
Galaxies Without Gas Clumping (112)				
Gas Fraction (%)	14.8	94.9	61.3 ± 19.5	63.2
Relative Error	-0.889	1.417	-0.028 ± 0.211	-2.56×10^{-7}

Several important trends emerge from these results. First, the clumping factor remains within physically reasonable bounds across the entire sample of 3048 kinematic points. Although the algorithm allows the parameter to vary across the full interval $[0, 1]$, no reconstructed configuration produces values below approximately 2% or above 94%.

Second, the galaxies that require gas clumping are precisely those with the lowest gas fractions. Their median gas fraction is approximately 17%, compared to about 63% for galaxies that do not require clumping. This behavior is physically expected: when the gas mass is small relative to the stellar component, a more concentrated distribution of the gas can significantly modify the gravitational binding energy.

Finally, the distribution of the relative error obtained without gas clumping shows a pronounced asymmetry. The error spans from approximately -0.89 to 14.5, indicating that the algorithm can easily generate configurations producing more gravitational binding energy than required by the inferred dark mass, whereas the opposite situation is comparatively rare. Taken together, these results suggest that the gas clumping parameter is not merely a numerical artifact introduced by the optimization procedure. Instead, its behavior across the dataset appears consistent with the presence of an underlying physical effect related to the spatial distribution of the gas component in galaxies.

6.3 Consequences of the Search Algorithm

The role of the search strategy can be examined by considering only the reconstruction of the final kinematic point of each of the 174 galaxies. In this simplified configuration, the algorithm performs only a linear greedy exploration while the gravitational binding energy is computed using the exact estimator. Even under this restricted setup, the method is capable of producing excellent dynamical reconstructions. This provides a useful framework to analyze how different strategies for selecting the optimization trajectory affect the statistical properties of the resulting stellar populations.

During the greedy exploration, several candidate modifications of the stellar fractions may produce a reduction of the relative error between the predicted gravitational binding energy and the inferred dark mass. The algorithm must therefore select which of these branches to follow. Four strategies are considered:

(i) the classical greedy approach, which selects the candidate producing the largest improvement in the dark-mass reconstruction;

(ii) a photometry-assisted strategy that selects, among candidates with dark-mass improvement, the one minimizing the photometric distance from the expected galaxy colors;

(iii) a random selection among all admissible improvements;

(iv) the null hypothesis, where stellar populations are drawn randomly within the allowed interval $P \pm k\sigma$ without any optimization.

The reconstruction performance obtained for these strategies is summarized in Table 9.

Table 9. Reconstruction performance for different search strategies.

Strategy	**Points Without Error**	**Galaxies Without Error**
Best greedy (dark mass)	170 (97.7%)	170 (97.7%)
Greedy + photometry	170 (97.7%)	170 (97.7%)
Random step	170 (97.7%)	170 (97.7%)
Null hypothesis	24 (13.8%)	24 (13.8%)

Remarkably, the three greedy-based strategies produce identical dynamical performance. Out of the 174 galaxies considered, 170 are reconstructed without error, corresponding to a success rate of 97.7%.

By contrast, the null hypothesis produces only 24 successful reconstructions, corresponding to 13.8%. This result confirms that the high success rate of the method cannot be attributed to random fluctuations within the allowed parameter space.

Although the dynamical performance is identical for the three greedy strategies, the photometric properties of the reconstructed stellar populations depend strongly on the trajectory selection rule. Table 10 summarizes the corresponding photometric correlations.

These results have an important methodological implication. The dynamical reconstruction itself is largely insensitive to the detailed choice of the search trajectory, as long as the gravitational constraint is enforced. Different strategies lead to nearly identical success rates for the dark-mass reconstruction, indicating that the dynamical solution is strongly constrained by the physical relation between gravitational binding energy and the baryonic mass distribution.

The search strategy therefore primarily affects the internal organization of the stellar populations rather than the global dynamical solution. In this sense, the algorithm acts mainly as a selector among the many stellar population configurations that satisfy the same gravitational constraint, shaping their photometric properties without altering the underlying dynamical consistency.

6.4 Inefficiency of Complex Search Strategies

The use of more complex optimization procedures, such as quadratic searches extending the linear greedy exploration, proves in practice to be counterproductive. In particular, these methods do not improve either the reconstruction of the dark mass or the recovery of realistic stellar populations.

Table 10. Correlation analysis between predicted and observed galaxy colors for different search strategies. Pearson r and Spearman ρ coefficients are reported together with their Gaussian-equivalent significances.

Strategy	Color	N	r_{P}	σ_{P}	ρ_{S}	σ_{S}
Best greedy (dark mass)	FUV–NUV	136	-0.214	2.53	-0.219	2.59
	$r-z$	171	0.094	1.23	0.380	5.34
	$g-r$	170	0.233	3.10	0.319	4.36
	NUV–r	138	0.314	3.85	0.636	9.62
Greedy + photometry	FUV–NUV	136	0.503	6.73	0.415	5.29
	$r-z$	171	0.007	0.09	0.136	1.78
	$g-r$	170	0.181	2.39	0.241	3.22
	NUV–r	138	0.220	2.63	0.572	8.13
Random step	FUV–NUV	136	-0.127	1.48	-0.137	1.60
	$r-z$	171	-0.056	0.73	0.108	1.41
	$g-r$	170	0.055	0.71	0.145	1.90
	NUV–r	138	0.130	1.53	0.246	2.95
Null hypothesis	FUV–NUV	136	-0.106	1.23	-0.095	1.10
	$r-z$	171	0.029	0.37	0.029	0.38
	$g-r$	170	-0.002	0.02	0.005	0.07
	NUV–r	138	-0.046	0.54	-0.100	1.17

Similarly, approaches based on propagating solutions sequentially from one kinematic point to the next tend to be computationally slow while providing little practical benefit. In practice, their performance does not exceed that obtained by simply selecting, for each galaxy, the single solution that minimizes the local relative error among all resolved points. This simplified strategy already achieves excellent results, as illustrated in Tables 6 and 7. The retained population for a galaxy therefore corresponds to the resolved point that minimizes its local relative error, independently of its radial position within the galaxy. More elaborate strategies attempting to enforce continuity along the rotation curve do not produce measurable improvements.

This preference for algorithmic simplicity is not unexpected. The underlying models governing both the dark-mass reconstruction and the photometric constraints are essentially linear, so additional layers of algorithmic complexity do not introduce new physical information and may instead hinder the efficiency of the optimization.

Taken together, the previous analyses highlight a common pattern: the success of the reconstruction does not rely on algorithmic sophistication but rather on the strength of the underlying physical constraint. Once the gravitational binding energy provides the correct dynamical scale, a wide range of simple search strategies are sufficient to identify consistent stellar populations. The algorithm therefore acts primarily as an exploration tool within a physically constrained parameter space, rather than as the source of the solution itself.

7 Conclusion

In this work, we examined the evaluation of effective gravitational binding energy in heterogeneous stellar systems and its implications for the reconstruction of galactic dark-mass profiles. The central result is that a physically consistent macroscopic estimator can be constructed from additive binding-energy contributions combined through volume-conserving mergers. This exact estimator is linear and permutation-invariant, and therefore provides a rigorous reference framework for relating baryonic structure to an effective dark-mass contribution.

By contrast, the heuristic formulation previously used evaluates the gravitational scale of partially assembled configurations at each aggregation step, thereby introducing a strong dependence on the ordering of stellar populations. A systematic exploration of permutations demonstrates that this path dependence can produce large variations in the reconstructed dark-to-baryonic mass ratio. Optimized orderings substantially reduce the resulting bias, producing error distributions that become nearly Gaussian and centered close to zero.

However, a controlled algorithmic analysis reveals that the apparent superiority of the heuristic formulation is partly artificial. When the heuristic value is used both for convergence and evaluation, its success rate is naturally inflated relative to the exact energy. Once the exact estimator is used directly during the optimization process, the reconstruction remains highly efficient. This demonstrates that the success of the method does not fundamentally rely on the heuristic approximation itself, but rather on the strength of the physical constraint imposed by gravitational binding energy.

Independent photometric validations provide an additional consistency check. Correlations with GALEX and SDSS colors confirm that the reconstructed stellar populations are not arbitrary and retain meaningful cross-galaxy ordering. At the same time, the comparison of search strategies shows that the detailed optimization path affects mainly the internal organization of stellar populations rather than the global dynamical solution. In this sense, the algorithm primarily acts as a selector among the many stellar population configurations compatible with the same gravitational constraint.

The explicit treatment of gas clumping further supports this interpretation. The clumping parameter remains within physically reasonable bounds and is preferentially required in systems with low gas fractions, consistent with the expectation that variations in the spatial distribution of gas can modify the effective gravitational binding energy budget.

A broader methodological lesson also emerges from this study. Increasing algorithmic sophistication does not improve the reconstruction: quadratic searches and propagation strategies are generally slower and less effective than simple linear greedy procedures. Once the correct dynamical scale is imposed by the exact gravitational binding energy, relatively simple search rules are sufficient to identify realistic stellar populations. The solution therefore appears to be primarily physical rather than algorithmic.

From an epistemological perspective, this analysis also illustrates a broader caution in scientific methodology. Just as developing theoretical physics without regard for phenomenological reality would be of limited value, the opposite approach can also be problematic: modifying a well-founded theoretical framework primarily to force agreement with observations may obscure the underlying physical structure. In retrospect, the heuristic formulation explored in our earlier work partly falls into this second category. While it proved useful as a numerical tool for exploring the parameter space, the present analysis shows that its apparent advantages arise mainly from algorithmic properties rather than from a more accurate physical description.

The exact estimator therefore provides the appropriate physical baseline for evaluating effective gravitational binding energy, while heuristic formulations should be regarded primarily as computational approximations. More generally, the present results suggest that once the correct physical constraint is identified, the role of the algorithm is not to create the solution but simply to reveal it.

Software availability

The C++ and Python programs used to perform all numerical calculations and generate the corresponding graphs are freely available at dark-mass-generator.sourceforge.io or at https://doi.org/10.6084/m9.figshare.31724332.

Funding

This research received no specific grant from any funding agency in the public, commercial, or not-for-profit sectors.

Competing interests

The author declares no competing interests.

Roles

The author conceived the study, performed the analysis, and wrote the manuscript.

References

[1] N. Poupart, "Dark mass is potential energy." Preprint available at FigShare (doi.org/10.6084/m9.figshare.30543407) and ResearchGate (doi.org/10.13140/RG.2.2.15355.43046), 2025.

[2] L. Brillouin, *L'enigme $E = Mc^2$: Energie potentielle et renormalisation de la masse*, *Journal de Physique* **25** (1964) .

[3] L. Brillouin, *The mass of a system of potential energy*, *Proceedings of the National Academy of Sciences of the United States of America* **53** (1965) .

[4] V.C. Rubin, J. Ford, W. Kent and N. Thonnard, *Rotational properties of 21 sc galaxies with a large range of luminosities and radii, from ngc 4605 (r = 4kpc) to ugc 2885 (r = 122kpc)*, *The Astrophysical Journal* **238** (1980) 471.

[5] A. Bosma, *The distribution and kinematics of neutral hydrogen in spiral galaxies of various morphological types*, Ph.D. thesis, Rijksuniversiteit Groningen, 1978.

[6] C.W. Misner, K.S. Thorne and J.A. Wheeler, *Gravitation*, W. H. Freeman (1973).

[7] T. Clifton, P.G. Ferreira, A. Padilla and C. Skordis, *Modified gravity and cosmology*, *Physics Reports* **513** (2012) 1.

[8] R.C. Tolman, *Relativity, Thermodynamics and Cosmology*, Oxford University Press (1934).

[9] A. Deur, *An explanation for dark matter and dark energy consistent with the standard model of particle physics and general relativity*, *European Physical Journal C* **79** (2019) 883.

[10] A. Deur, C. Sargent and B. Terzic, *Significance of gravitational nonlinearities on the dynamics of disk galaxies*, *The Astrophysical Journal* **896** (2020) 94.

[11] A. Deur, *Relativistic corrections to the rotation curves of disk galaxies*, *European Physical Journal C* **81** (2021) 213.

[12] A. Deur, *Effect of the field self-interaction of general relativity on the cosmic microwave background anisotropies*, *Classical and Quantum Gravity* **39** (2022) 135003.

[13] F. Lelli, S.S. McGaugh and J.M. Schombert, *Sparc: Mass models for 175 disk galaxies with spitzer photometry and accurate rotation curves*, *The Astronomical Journal* **152** (2016) 157.

[14] N. Poupart, "Stellar population ordering from galactic dynamics." Preprint available at FigShare (doi.org/10.6084/m9.figshare.31175302) and ResearchGate (doi.org/10.13140/RG.2.2.35654.74561), 2026.

[15] D.C. Martin et al., *The galaxy evolution explorer: A space ultraviolet survey mission*, *The Astrophysical Journal Letters* **619** (2005) L1.

[16] L. Bianchi et al., "Galex gr5 x sdss dr7 matched catalogs." MAST / STScI High-Level Science Products, 2011.

[17] D.G. York et al., *The sloan digital sky survey: Technical summary*, *The Astronomical Journal* **120** (2000) 1579.

[18] M. Fukugita, T. Ichikawa, J.E. Gunn, M. Doi, K. Shimasaku and D.P. Schneider, *The sloan digital sky survey photometric system*, *The Astronomical Journal* **111** (1996) 1748.